A High Peak Output Power and High Power Conversion Efficiency SIMIMO Converter Using Optimal ON-Time Control and Hybrid Zero Current Switching for Energy Harvesting Systems in IoT Applications

Jae-Hyung Jung, *Student Member, IEEE*, Young-Ho Jung, *Member, IEEE*, Seong-Kwan Hong, *Member, IEEE*, and Oh-Kyong Kwon, *Member, IEEE*

***Abstract*—This article proposes a single inductor multi-input multioutput (SIMIMO) converter with high peak output power and power conversion efficiency for energy harvesting systems in Internet of Things (IoT) applications. The proposed SIMIMO converter consists of inputs with four harvesters and a battery, and outputs with 1.8 V output, 3.3 V output, and a battery. The optimal ON-time control method is proposed to optimally adjust the on time required to energize the inductor, thus increasing the peak output power to cover a wide distance range. In addition, the hybrid zero-current-switching (ZCS) method is proposed to adaptively calibrate the offset of the ZCS comparator, thus improving the power conversion efficiency. The proposed SIMIMO converter is fabricated using 0.18-μm standard bipolar-CMOS-DMOS (BCD) process technology with 1.8- and 5-V devices. The measurement results show that the peak output power is achieved to be 462 mW, and the peak power conversion efficiencies at 1.8 V output, 3.3 V output, and battery are 89.2%, 84.5%, and 86.4%, respectively. Moreover, the quiescent current of the power management controller, which controls the proposed converter, is achieved to be only 1.6 μA. Therefore, the proposed SIMIMO converter is suitable for energy harvesting systems in various IoT applications.**

***Index Terms*—Battery charger, energy harvesting, energy management, power integrated circuits.**

I. Introduction

THE Internet of Things (IoT) has been increasingly adopted in various applications such as building and home automation, industrial management systems, health care systems, smart grid systems, and wearable mobile devices [1]–[3]. Since the IoT devices have a limited usage time due to the limited battery power, they are required to operate with a very low average power, ranging from several microwatts to milliwatts. However, as the IoT devices have adopted high-performance sensors to cover a wide distance range, their peak power consumption has gradually increased up to hundreds of milliwatts in recent low-power wide-area applications such as long-range (LoRa) [3] and narrowband internet of things (NB-IoT) [4]–[6], thus requiring high peak output power for loads. Since such IoT devices are usually installed in not-easily-accessible places, they need to maintain a necessary operating power level without frequently replacing the battery. Thus, the energy harvesting systems, which use the harvesters as inputs to obtain energies from the ambient environment such as light [7], heat [8], vibration [9], and RF [10], have become increasingly useful for IoT applications. However, since the harvested energies are generally sensitive to the surroundings, the multienergy harvesting systems need to sufficiently collect the energy from various harvesters allowing them to achieve high system efficiency and reliability in applications [16].

To meet the abovementioned requirements, various multi-input energy harvesting structures have been reported [11]–[17]. The power ORing structure in [11] and [12], which is the simplest architecture, combines energies obtained from multi-harvesters by connecting all the harvesters in parallel through diodes. However, it uses only the highest voltage as an input energy source, resulting in a low power conversion efficiency. The two-stage converter structure in [13] and [14], which is an inductor-based time-multiplexing switching converter, transfers its input energies obtained from multiharvesters to its storage devices using the first-stage converter and regulates its output voltage using the second-stage converter. However, its dual conversion causes a decrease in the overall power conversion efficiency from the input harvester to the output load. The dual-path converter structure in [15]–[17] transfers the harvested energies to both the storage device and the load. The converter structure in [16] shares an inductor by adopting a prescheduled time slot and maximizes the power transfer to the output load using a maximum power point tracking (MPPT) method. However, it can achieve high efficiency only when it operates in the prescheduled time slot. The converter structure in [17] ensures the stability by

Manuscript received July 9, 2019; revised November 10, 2019; accepted December 25, 2019. Date of publication December 31, 2019; date of current version April 22, 2020. Recommended for publication by Associate Editor M. D. Seeman. *(Corresponding author: Oh-Kyong Kwon.)*

The authors are with the Hanyang University, Seoul 133-791, South Korea (e-mail: eveut@hanyang.ac.kr; wario2@hanyang.ac.kr; seongkhong@hanyang.ac.kr; okwon@hanyang.ac.kr).

Color versions of one or more of the figures in this article are available online at http://ieeexplore.ieee.org.

Digital Object Identifier 10.1109/TPEL.2019.2963513

using error amplifiers and comparators, but consumes a large amount of static power. To solve the aforementioned problems, various control methods for converters have been studied to achieve high efficiency, low quiescent current, and high peak output power [18]–[22].

First, to achieve the high conversion efficiency and low power consumption, zero-current-switching (ZCS) control methods have been researched [18]–[20]. In [18], a digitally controlled ZCS method achieves a high power conversion efficiency in discontinuous conduction mode (DCM) by adjusting the de-energizing time period using an incrementer and decrementer logic, but its input and output voltage ranges are limited due to the timing control. In [19] and [20], the ZCS method with an analog comparator is implemented to extend the input and output voltage ranges by comparing the drain and source voltages of the switch. However, the offset of the comparator itself causes high power consumption and low power conversion efficiency.

Second, to minimize the quiescent current and increase the input voltage range and peak output power in single inductor multiport multi-input–multi-output (SIMIMO) converter, ON-time control methods have been researched. The single inductor multiport converters operate in only one mode for each switching period with different input voltage, output voltage, harvested input power, and output load power according to harvesters and output load conditions. In addition, they operate only in DCM using the constant ON-time (COT) or adaptive ON-time (AOT) control methods to avoid the influence of the remaining inductor current on the next operation mode for low power consumption. The COT methods with pulse-frequency and pulse-skipping modulation [21], and energy recycling [30] are employed not only to minimize the quiescent current, but also to improve the power conversion efficiency. However, these works can operate only with fixed on time and fixed input voltage, resulting in decreases in the input voltage range and peak output power. To overcome the above issues, several AOT control methods have been researched. In [16], the AOT control method with the adaptive switching frequency according to the harvester types is employed to control the on time during a prescheduled time slot, thus increasing the input voltage range. However, this AOT method can achieve high efficiency only when it operates in the prescheduled time slot. In [14], the AOT control method with the wide input voltage range is employed to increase the input voltage range by comparing the harvester input voltage with the MPP voltage of the harvester. However, each harvester requires a different capacitor with capacitance value, of which is greater than 100 μF, and an inductor with an inductance value of 10 mH to secure the adaptive on time according to the input voltage. Moreover, it needs a frequent adjustment of the capacitance and inductance values when the input voltage is changed. In [28] and [29], the AOT control method using an adaptive ON-time generator including the adaptive peak inductor current controller is employed to automatically adjust the on time according to the input voltage. However, this AOT method cannot increase or decrease the on time according to the load current, resulting in a decrease in the peak output power. In [22], the AOT method further increases the peak output power by increasing or decreasing the on time according to the output load current, but suffers from the low input and output voltage ranges, and low peak output power, which are limited to only 1.8 and 1.4 V, and 60 mW, respectively, which are not suitable for IoT applications requiring high peak output power. As aforementioned, previously reported state-of-the-art works still have various issues in improving the performance to be applied to the energy harvesting systems in IoT applications.

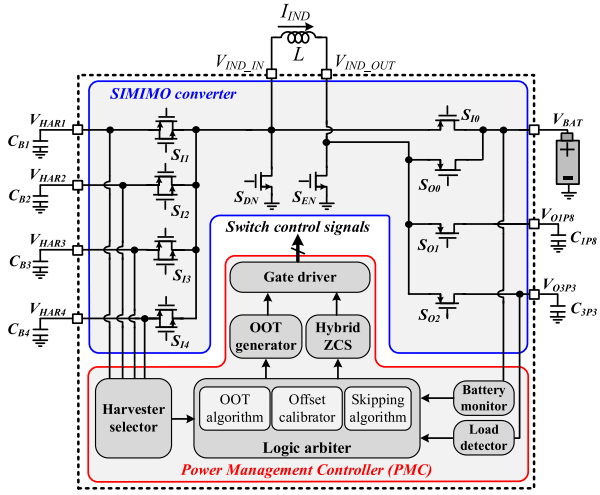

Fig. 1. Block diagram of the proposed energy harvesting system including the SIMIMO converter and PMC.

In this article, a SIMIMO converter using an optimal ON-time (OOT) control method with a hybrid ZCS method is proposed to improve the input and output regulation characteristics, peak output power, input and output voltage ranges, and power conversion efficiency. The proposed SIMIMO converter, which employs the dual-path converter structure and MPPT method for each harvester, is controlled by 15 operation modes according to the combination of multi-inputs (four harvesters and a battery) and multioutputs (1.8 V output, 3.3 V output, and a battery). The proposed OOT control method adaptively optimizes the on time required to energize the inductor, thus improving the input and output regulation characteristics, and peak output power. The proposed hybrid ZCS employs an offset calibration to achieve high power conversion efficiency.

This article is organized as follows. Section II describes the architecture and operation principle of the proposed SIMIMO converter with the power management controller (PMC). Section III presents the proposed OOT generator with the OOT and skipping algorithms. Section IV presents the proposed hybrid ZCS with offset calibration. In Section V, the circuit implementation of the proposed SIMIMO converter is explained in detail. In Section VI, the experimental results are analyzed and compared with prior works. Finally, the conclusion is given in Section VII.

II. Architecture and Operation Principle of the Proposed SIMIMO Converter With PMC

A. Architecture of the Proposed SIMIMO Converter

Fig. 1 shows the block diagram of the proposed energy harvesting system including the SIMIMO converter and PMC, which obtains the energies from the multi-input harvesters or the battery and then transfers the harvested energies to the outputs or

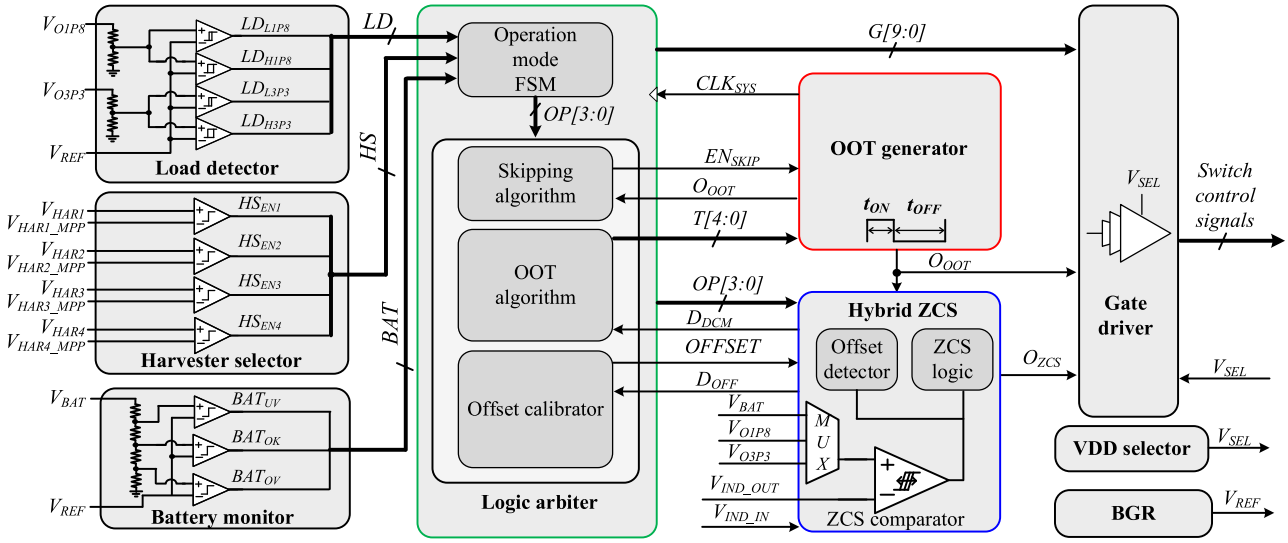

Fig. 2. Block diagram of the proposed PMC.

the battery. The proposed SIMIMO converter has the inputs consisting of $V_{\rm BAT}$, and $V_{\rm HAR1}$, $V_{\rm HAR2}$, $V_{\rm HAR3}$, and $V_{\rm HAR4}$, which represent a battery and multiharvesters such as the photovoltaic, thermoelectric, RF, and piezoelectric, respectively. It also has the outputs consisting of V_{O1P8} for 1.8-V output, V_{O3P3} for 3.3-V output, and $V_{\rm BAT}$. The PMC generates the switch control signals to control the switches in the SIMIMO converter, thus not only efficiently transferring the harvested energies to the V_{O1P8} and V_{O3P3} or the $V_{\rm BAT}$, but also accurately regulating the V_{O1P8} and V_{O3P3} by the buck or buck–boost operation.

The proposed converter includes the input power switches (S_{I0} for the battery and S_{I1}–S_{I4} for the harvesters) and output power switches (S_{O0} for the battery, S_{O1} for V_{O1P8}, and S_{O2} for V_{O3P3}). Here, S_{I1}–S_{I4} are implemented with transmission gates instead of using NMOS or PMOS in order to have a wide input voltage range. S_{EN} and S_{DN} are the switches to energize and de-energize the inductor (L) so as to increase and decrease the inductor current ($I_{\rm IND}$), respectively. All the above ten switches are controlled by the switch control signals generated from the PMC. C_{B1}–C_{B4} are used as buffers for the respective harvesters for MPPT operation, and C_{1P8} and C_{3P3} are used as output capacitors to ensure the stable output regulation.

The proposed converter transfers the harvested energy in four ways: the battery-to-load, harvester-to-load, harvester-to-battery, and freewheeling modes, according to the combination of the multi-inputs (V_{HAR1}, $V_{\rm HAR2}$, $V_{\rm HAR3}$, $V_{\rm HAR4}$, and $V_{\rm BAT}$) and multioutputs (V_{O1P8}, V_{O3P3}, and $V_{\rm BAT}$). In the battery-to-load mode, the energy is transferred from the battery to the load in two operation modes according to the combination of $V_{\rm BAT}$ and the output load (V_{O1P8} or V_{O3P3}). In the harvester-to-load mode, the energy is transferred from the harvester to the output load in eight operation modes according to combination of the harvester ($V_{\rm HAR1}$, $V_{\rm HAR2}$, $V_{\rm HAR3}$, or $V_{\rm HAR4}$) and the output load (V_{O1P8} or V_{O3P3}). In the harvester-to-battery mode, the energy is transferred from the harvester to the battery in four operation modes according to the combination of the harvester ($V_{\rm HAR1}$, $V_{\rm HAR2}$, $V_{\rm HAR3}$, or $V_{\rm HAR4}$) and $V_{\rm BAT}$. In the freewheeling mode, all ten switches in the proposed converter are turned OFF, and thus no energy is transferred from the input to the output load. Among the above 15 operation modes, only one mode is operated during each switching period depending on the operation of the ten switches, which are controlled by the PMC.

B. PMC for the Proposed SIMIMO Converter

Fig. 2 shows the block diagram of the proposed PMC, which consists of a load detector, harvester selector, battery monitor, logic arbiter, OOT generator, hybrid ZCS, gate driver, VDD selector, and bandgap reference generator (BGR).

The load detector, which has two kinds of comparators with high and low hysteresis, compares the resistor-divided V_{O1P8} and V_{O3P3} with a reference voltage ($V_{\rm REF}$), and determines the output load condition according to its output (LD) by monitoring whether V_{O1P8} and V_{O3P3} are regulated [20]. Here, LD consists of LD_{H1P8} and LD_{L1P8} for V_{O1P8}, and LD_{H3P3} and LD_{L3P3} for V_{O3P3}, each pair of which is produced from the high and low hysteresis comparators, respectively. In this article, the high and low hysteresis comparators are employed to determine the output load condition, which can be represented as "light" or "heavy" depending on whether the power consumption at the output load of the proposed converter is less or greater than the harvested input power, respectively. If both LD_{H1P8} and LD_{H3P3} are high, the output load is considered as under the light-load condition, and otherwise it is considered as under the heavy-load condition.

Under the light-load condition, if one or both of LD_{L1P8} and LD_{L3P3} are low, the harvested input power is supplied to the output loads of V_{O1P8} and V_{O3P3}. Otherwise, the harvested input power remaining after fully supplying the power to the output loads charges the battery.

Under the heavy-load condition, if both LD_{L1P8} and LD_{L3P3} are high, the harvested input power is supplied to the output loads. Otherwise, the harvested input power is insufficient to drive the output load of V_{O1P8} or V_{O3P3}, and thus the battery supplies the required amount of power to the output loads.

Unlike the conventional feedback loop used in the voltage and current modes, which has a compensator to stabilize the converter in continuous conduction mode (CCM) and DCM, this hysteretic mode used in the proposed converter does not require a compensation scheme for stability because the gain and bandwidth in the hysteretic mode are theoretically infinite [33].

The harvester selector compares the input voltage of the harvesters ($V_{\rm HAR1}$, $V_{\rm HAR2}$, $V_{\rm HAR3}$, and $V_{\rm HAR4}$) with their corresponding $V_{\rm MPP}s$ ($V_{HAR1\_{\rm MPP}}$, $V_{HAR2\_{\rm MPP}}$, $V_{HAR3\_{\rm MPP}}$, and $V_{HAR4\_{\rm MPP}}$), respectively. It then produces its output (*HS*), which consists of HS_{EN1}, HS_{EN2}, HS_{EN3}, and HS_{EN4}. When one of *HS* becomes high, its corresponding harvester will be selected as the input of the proposed converter based on the MPPT. A simple open-circuit voltage method [32] is employed in the proposed SIMIMO converter to accurately track the MPP, while achieving low power consumption for IoT applications. Depending on the harvester type, $V_{\rm MPP}$ of each harvester has a different sampling percentage of its open-circuit voltage ($V_{\rm OC}$). $V_{\rm MPP}$ of the thermoelectric, RF, and piezoelectric harvesters, which are modeled as linear elements, has a sampling percentage of 50% of its $V_{\rm OC}$, whereas $V_{\rm MPP}$ of the photovoltaic harvester, which is model as nonlinear elements, has a sampling percentage of 70% of its $V_{\rm OC}$.

The battery monitor compares the resistor-divided $V_{\rm BAT}$ with $V_{\rm REF}$ and determines the $V_{\rm BAT}$ state according to the compared result (*BAT*), which consists of ${\rm BAT_{OV}}$, ${\rm BAT_{OK}}$, and ${\rm BAT_{UV}}$. Depending on whether ${\rm BAT_{OV}}$, ${\rm BAT_{OK}}$, or ${\rm BAT_{UV}}$ is high, the $V_{\rm BAT}$ state is determined to be overvoltage, OK voltage, or undervoltage state, respectively. If all the resistor-divided $V_{{\rm BAT}s}$ are less than $V_{\rm REF}$, the battery is considered as in the undervoltage state, and the harvester then charges the battery without regulating V_{O1P8} or V_{O3P3}. If all the resistor-divided $V_{{\rm BAT}s}$ are greater than $V_{\rm REF}$, the battery is considered as in the overvoltage state, and the harvester and battery then regulate both V_{O3P3} and V_{O1P8} under the heavy-load condition. Otherwise, the battery is considered as in the OK-voltage state, and the harvester and battery then regulate both V_{O3P3} and V_{O1P8} under the heavy-load condition, while the surplus power in the harvester charges the battery under the light-load condition. To protect the battery, the $V_{\rm BAT}$ is periodically monitored to be greater than the undervoltage and less than the overvoltage.

The logic arbiter, which is implemented through logic synthesis, employs the finite-state machine (FSM) to determine the 15 operation modes of the proposed converter according to the load condition of *LD*, the selected harvester of *HS*, and the battery state of *BAT*. The 15 operation modes can be represented as *OP[3:0]*, each of which drives the OOT and skipping algorithms, and the offset calibrator. Here, each *OP[3:0]* has its own register value that is continuously updated as the OOT algorithm is performed. The OOT algorithm provides an $(n+1)$-bit control signal, *T[n:0]*, which is determined by the register value of *OP[3:0]*, to the OOT generator in order to adjust the on time required to energize the inductor ($t_{\rm ON}$). Here, *n* is a bit resolution for controlling the $t_{\rm ON}$, which is determined according to the allowable variations in V_{O3P3} and V_{O1P8}, representing how much $t_{\rm ON}$ can be adjusted. In this article, *n* is selected to be 4 considering 10% allowable variations in V_{O3P3} and V_{O1P8}. The skipping algorithm provides a control signal, $EN_{\rm SKIP}$, to the OOT generator in order to optimally control the number of $O_{\rm OOT}$ skippings according to the load condition, where $O_{\rm OOT}$, which is generated by the OOT generator, is a pulse signal with a width of $t_{\rm ON}$. Here, the $O_{\rm OOT}$ remaining after skipping is used as a system clock signal, $CLK_{\rm SYS}$. The skipping algorithm controls $EN_{\rm SKIP}$ to produce more (less) $O_{\rm OOT}$ skippings under the light (heavy) condition, thus decreasing (increasing) the number of $CLK_{\rm SYS}$ occurrences, respectively, resulting in optimally improving the power consumption and regulation characteristics. The offset calibrator generates an offset signal, *OFFSET*, which is enabled to adaptively calibrate the offset voltage of the ZCS comparator in the hybrid ZCS. The gate signals, *G[9:0]*, which control the gate driver, are activated according to *OP[3:0]* in order to determine which power switches of the SIMIMO converter are turned ON or OFF using the highest voltage selected from among the V_{O1P8}, V_{O3P3}, and $V_{\rm BAT}$ ($V_{\rm SEL}$), which is selected by the VDD selector.

The proposed OOT generator produces $O_{\rm OOT}$ and $CLK_{\rm SYS}$. The $O_{\rm OOT}$ activates the hybrid ZCS to control the $I_{\rm IND}$ for efficient energy delivery and determine whether the proposed converter operates in DCM or CCM. It also controls the gate driver along with *G[9:0]* and the hybrid ZCS output ($O_{\rm ZCS}$), and thus the $t_{\rm ON}$ of the switch control signals can be optimally adjusted.

The proposed hybrid ZCS is implemented to efficiently control the energy transfer operation. It turns on one of the output power switches when the $I_{\rm IND}$ starts to de-energize the inductor, and thus the energy is transferred to the output load. It also turns off one of the output power switches when the $I_{\rm IND}$ becomes zero, and thus the energy is no longer transferred to the output load. In addition, the proposed hybrid ZCS detects the positive or negative offset voltage of the ZCS comparator, which causes a body diode current or reverse leakage current, depending on whether the ZCS comparator operates before or after the $I_{\rm IND}$ becomes zero, respectively. The offset calibrator in the logic arbiter then performs the offset calibration using *OFFSET*, thus enabling the ZCS comparator to accurately detect the moment when the $I_{\rm IND}$ becomes zero. Moreover, it monitors the $I_{\rm IND}$ and limits the increase in $t_{\rm ON}$ to make the proposed converter always operate in DCM, thus achieving a high peak harvested input power and the peak output power for load in DCM.

III. OOT Generator and Algorithms

A. OOT Generator

Fig. 3(a) shows the block diagram of the proposed OOT generator including the OOT core and pulse skipper driven by the OOT and skipping algorithms, respectively. Fig. 3(b) shows the proposed OOT core, which consists of a sub-VDD regulator and variable ON-time generator. The sub-VDD regulator provides a

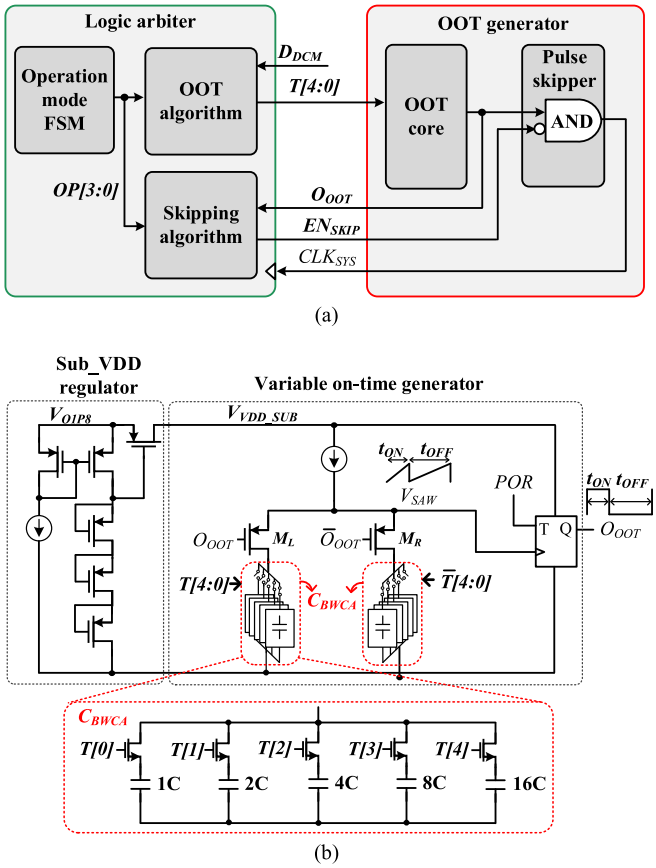

Fig. 3. (a) Block diagram of the proposed OOT generator and (b) schematic diagram of the proposed OOT core.

subvoltage ($V_{\mathrm{VDD\_SUB}}$) of 1 V, which is less than a V_{O1P8} of 1.8 V, to the variable ON-time generator to minimize the power consumption. The variable ON-time generator produces O_{OOT} with a fixed period of ($t_{\mathrm{ON}} + t_{\mathrm{OFF}}$). Here, t_{ON} or off-time (t_{OFF}) is, respectively, determined according to the duration of the sawtooth signal (V_{SAW}) when M_L or M_R is turned ON as the T flip–flop toggles O_{OOT} at a V_{SAW} of higher than a logic threshold voltage, which is about 0.5 V in this work. The V_{SAW} duration for t_{ON} or t_{OFF} is determined by the charging time of the binary weighted capacitor array (C_{BWCA}), as shown in Fig. 3(b), which is adjusted by controlling the capacitance values in the C_{BWCA} according to *T[4:0]* and its inverted signal $\overline{T}$ *([4:0])*, respectively. In this way, the variable ON-time generator can adjust the t_{ON} of O_{OOT} according to *T[4:0]*, thus controlling the amount of the I_{IND}, resulting in an efficient energy delivery. The power on rest is used as the input of the T flip-flop to prevent a phase shift of O_{OOT}.

The pulse skipper, which is controlled by EN_{SKIP} of the skipping algorithm, skips O_{OOT} under the light-load condition to reduce the power consumption of the PMC. When EN_{SKIP} becomes high under the light-load condition, the pulse skipper skips O_{OOT}, whereas when EN_{SKIP} becomes low under the heavy-load condition, O_{OOT} remains as it is. Since the O_{OOT} remaining after skipping is used as CLK_{SYS}, the number of CLK_{SYS} occurrences decreases as more O_{OOT} skippings occur under the light-load condition, and thus the total power consumption of the PMC decreases because the PMC is activated at the positive edge of CLK_{SYS}. However, the regulation characteristics are degraded due to decrease in CLK_{SYS} occurrences. Therefore, the proposed skipping algorithm, which will be explained in Section III.C, is implemented to adjust the number of O_{OOT} skippings so as to optimally improve the power consumption under the light-load condition and the regulation characteristics under the heavy-load condition.

B. OOT Algorithm

In the conventional COT method [21], as t_{ON} increases, the peak harvested input power and the peak output power increase, but the undershoot and overshoot voltages increase at the input and output, respectively, thus degrading the regulation characteristics. On the contrary, as t_{ON} decreases, the ripple voltage at the output decreases, but the switching loss increases, thus decreasing the power conversion efficiency under the light-load condition. Therefore, t_{ON} should be optimally adjusted to improve the regulation characteristics, and the peak harvested input power and the peak output power.

In the proposed SIMIMO converter, when more power is needed at the output load, the same operation mode is repeated to increase t_{ON}, and the inductor peak current ($I_{\mathrm{IND\_PEAK}}$), which is controlled by adjusting t_{ON}, increases, thus transferring more power to the output load. If t_{ON} is too long, too much energy is transferred to the output loads, and thus the overshoot voltage ($\Delta V_{\mathrm{OUT\_OVER}}$) and undershoot voltage ($\Delta V_{\mathrm{IN\_UNDER}}$) occur at the output and input of the proposed converter, respectively, resulting in a degradation in the regulation characteristics. On the other hand, if t_{ON} is too short, too little energy is transferred to the output loads, and thus the proposed converter takes a long transient time, resulting in a degradation in the regulation characteristics, and a decrease in the peak harvested input power and the peak output power. Therefore, the OOT algorithm, which can optimally adjust the number of *OP[3:0]* repetitions (N_T), is implemented to optimally adjust t_{ON} so as to optimize regulation characteristics and the peak harvested input power and the peak output power.

Fig. 4 shows the flowchart of the proposed OOT algorithm, which takes *OP[3:0]* and D_{DCM} as inputs, and produces *T[4:0]* as an output, as depicted in Fig. 3(a). Here, D_{DCM} is a signal provided from the hybrid ZCS, which determines whether the proposed converter is in DCM or CCM.

The OOT algorithm starts with the initial values ($OP[3:0]_{\mathrm{PREV}}$ = freewheeling mode, $N_T = 1$, and all the initial register values of *OP[3:0]* = 5'b00000).

When CLK_{SYS} occurs at the positive edge, the FSM determines *OP[3:0]* according to the load condition of *LD*, the selected harvester of *HS*, and the battery state of *BAT*, and assigns it to $OP[3:0]_{\mathrm{CRNT}}$, which is a current *OP[3:0]*. Then, the OOT algorithm checks whether the operation mode is repeated or not by comparing $OP[3:0]_{\mathrm{CRNT}}$ with $OP[3:0]_{\mathrm{PREV}}$, which is a previous *OP[3:0]* before one clock.

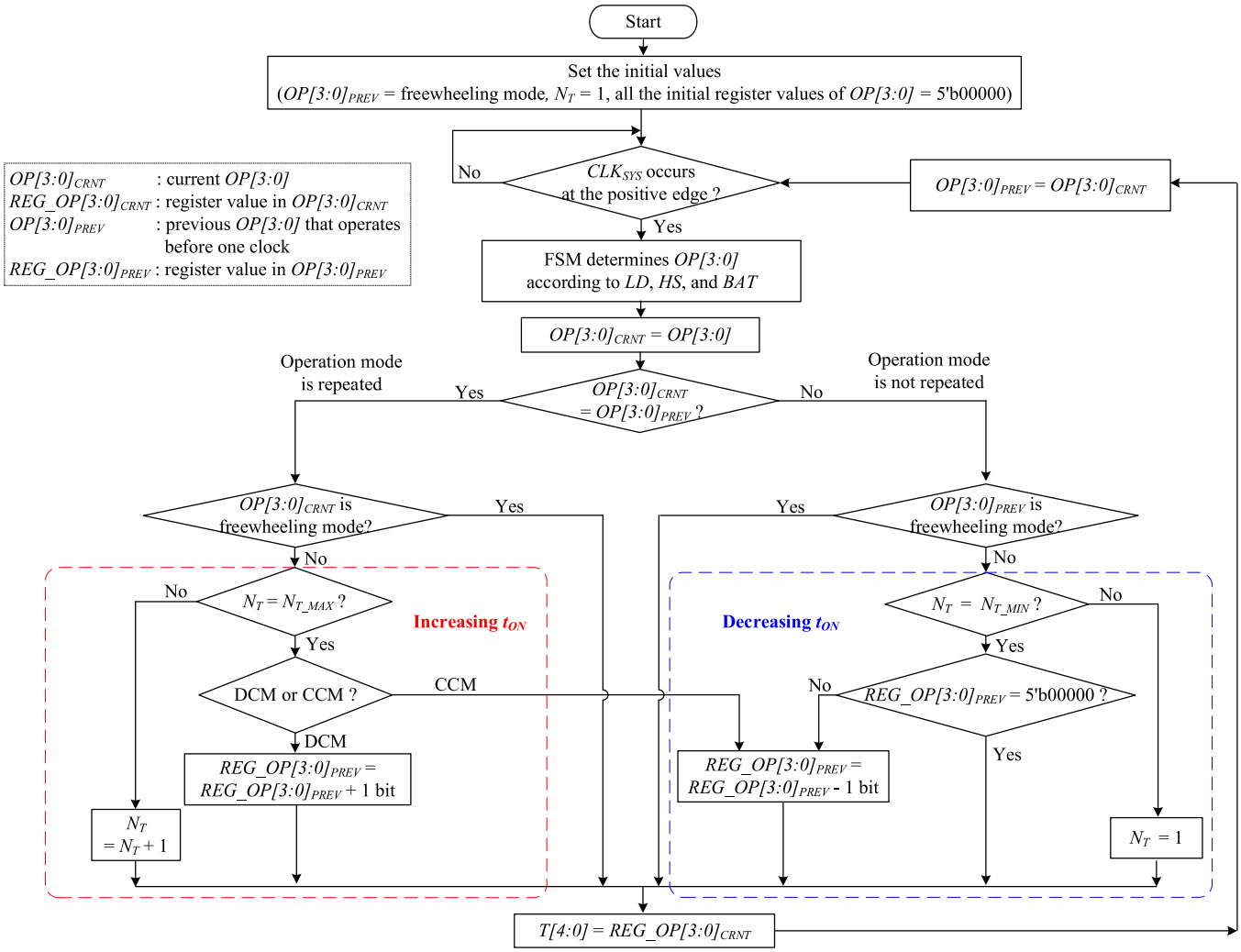

Fig. 4. Flowchart of the proposed OOT algorithm.

When $OP[3:0]_{\mathrm{CRNT}}$ is equal to $OP[3:0]_{\mathrm{PREV}}$, which represents that the operation mode is repeated for more power, if $OP[3:0]_{\mathrm{CRNT}}$ is a freewheeling mode, $REG\_OP[3:0]_{\mathrm{PREV}}$, which is a register value of $OP[3:0]_{\mathrm{PREV}}$, remains as it is, and thus, $T[4:0]$ is not changed. Otherwise, N_T is compared with N_{T_MAX}. Here, N_{T_MAX} is a maximum value of N_T, which is determined considering the tradeoff between the peak harvested input power and the peak output power, and regulation characteristics. If N_T is equal to N_{T_MAX}, the OOT algorithm checks DCM or CCM, which is determined by the hybrid ZCS, which will be explained in Section IV. When DCM is detected, the OOT algorithm increases $REG\_OP[3:0]_{\mathrm{PREV}}$ by 1 bit, and updates $T[4:0]$ to $REG\_OP[3:0]_{\mathrm{CRNT}}$, which is a register value of $OP[3:0]_{\mathrm{CRNT}}$. This operation is repeated until CCM is detected. When CCM is detected, the OOT algorithm decreases $REG\_OP[3:0]_{\mathrm{PREV}}$ by 1 bit, thus making the proposed converter always operate in DCM. If N_T is not equal to N_{T_MAX}, N_T increases by 1, while $T[4:0]$ remains as it is. In this way, when t_{ON} is too short, the OOT algorithm increases $T[4:0]$ in DCM by increasing the register values of $OP[3:0]$, resulting in an increase in t_{ON}.

When $OP[3:0]_{\mathrm{CRNT}}$ is not equal to $OP[3:0]_{\mathrm{PREV}}$, which represents that the operation mode is not repeated, if $OP[3:0]_{\mathrm{PREV}}$ is a freewheeling mode, $REG\_OP[3:0]_{\mathrm{PREV}}$ remains as it is, while $T[4:0]$ is updated to $REG\_OP[3:0]_{\mathrm{CRNT}}$. Otherwise N_T is compared with N_{T_MIN}, which is a minimum value of N_T. If N_T is equal to N_{T_MIN}, $REG\_OP[3:0]_{\mathrm{PREV}}$ is compared with 5'b00000; otherwise, N_T becomes 1. If $REG\_OP[3:0]_{\mathrm{PREV}}$ is equal to 5'b00000, $REG\_OP[3:0]_{\mathrm{PREV}}$ remains as it is; otherwise, $REG\_OP[3:0]_{\mathrm{PREV}}$ decreases by 1 bit. $T[4:0]$ is then updated to $REG\_OP[3:0]_{\mathrm{CRNT}}$. In this way, when t_{ON} is too long, the OOT algorithm decreases $T[4:0]$ by decreasing the register values of $OP[3:0]$, resulting in an decrease in t_{ON}.

As described above, the proposed OOT algorithm repeatedly adjusts t_{ON} by updating $T[4:0]$ according to the register values of $OP[3:0]$, while controlling N_T to be greater than N_{T_MIN} and less than N_{T_MAX}, resulting in an optimal t_{ON}. In this work, N_{T_MIN} was determined to be greater than 1 to protect the occurrence of the undershoot and overshoot voltage at the output and input of the proposed converter, respectively. In addition, N_{T_MAX} was determined to be as low as possible

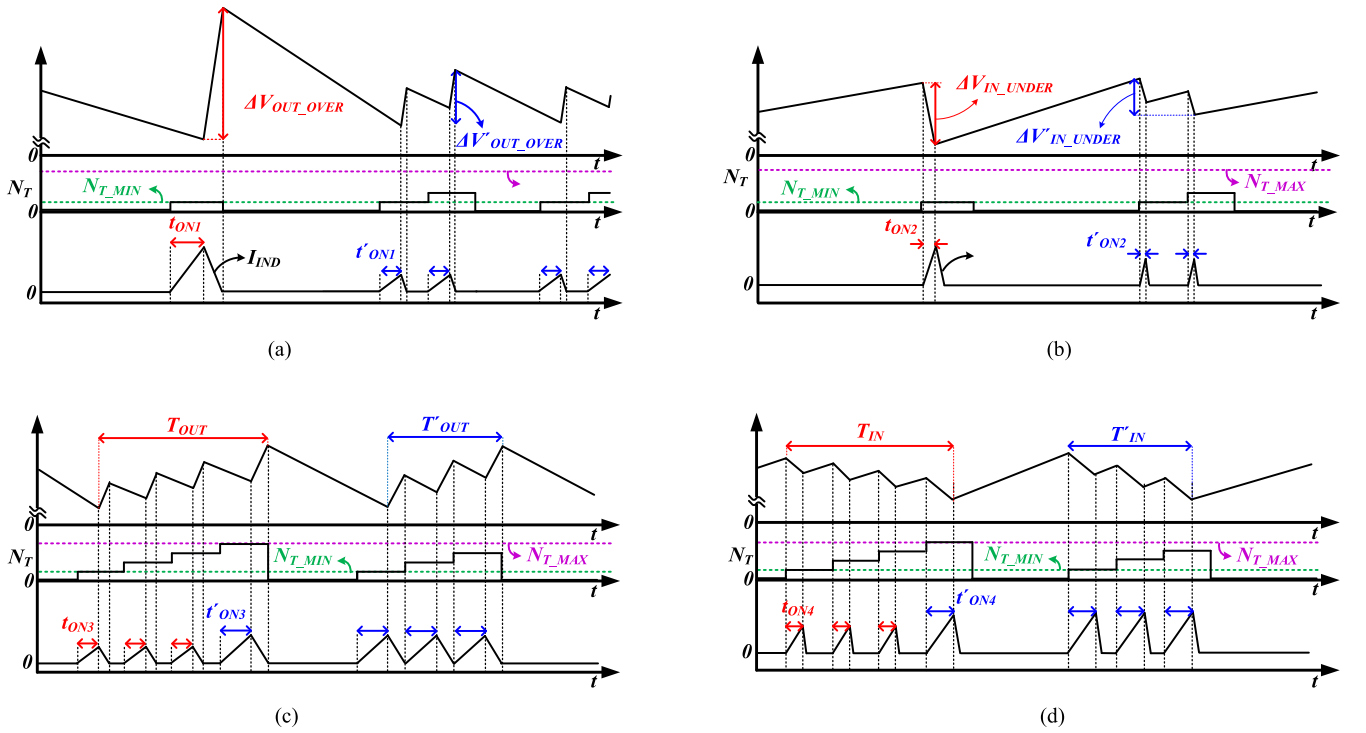

Fig. 5. Timing diagram of input and output voltages of the proposed converter using the proposed OOT algorithm (a) when the overshoot voltage occurs at the output at an N_T of N_{T_MIN}, (b) when the undershoot voltage occurs at the input at an N_T of N_{T_MIN}, (c) when the transient time at the output is long at an N_T of N_{T_MAX}, and (d) when the transient time at the input is long at an N_T of N_{T_MAX}.

to improve the transient response and ripple voltage at the output.

Fig. 5 shows the timing diagram of the harvester input, V_{HAR}, and the output, V_{O1P8} or V_{O3P3}, of the proposed converter according to N_T, while controlling t_{ON} for high regulation characteristics.

As N_T approaches N_{T_MIN}, indicating that t_{ON} is too long, $\Delta V_{\mathrm{OUT\_OVER}}$ or $\Delta V_{\mathrm{IN\_UNDER}}$ occurs at the output or input of the proposed converter, as shown in Fig. 5(a) and (b), respectively. When $\Delta V_{\mathrm{OUT\_OVER}}$ occurs at the output, the OOT algorithm decreases t_{ON} from t_{ON1} to t'_{ON1} at an N_T between $N_{T\_\mathrm{MIN}}+1$ and $N_{T\_\mathrm{MAX}}-1$, thus reducing $\Delta V_{\mathrm{OUT\_OVER}}$ to $\Delta V'_{\mathrm{OUT\_OVER}}$, as shown in Fig. 5(a), resulting in decreasing the output ripple voltage. In the same manner, when $\Delta V_{\mathrm{IN\_UNDER}}$ occurs at the input, the OOT algorithm decreases t_{ON} from t_{ON2} to t'_{ON2} at an N_T between $N_{T\_\mathrm{MIN}}+1$ and $N_{T\_\mathrm{MAX}}-1$, thus reducing $\Delta V_{\mathrm{IN\_UNDER}}$ to $\Delta V'_{\mathrm{IN\_UNDER}}$, as shown in Fig. 5(b), resulting in decreasing the input ripple voltage.

As N_T approaches N_{T_MAX}, indicating that t_{ON} is too short, the proposed converter takes a long transient time for regulation at the output (T_{OUT}) and input (T_{IN}), as shown in Fig. 5(c) and (d), respectively. When T_{OUT} at the output is too long, the OOT algorithm increases t_{ON} from t_{ON3} to t'_{ON3} at an N_T between $N_{T\_\mathrm{MIN}}+1$ and $N_{T\_\mathrm{MAX}}-1$, thus reducing T_{OUT} to T'_{OUT}, as shown in Fig. 5(c), resulting in decreasing the output transient time. In the same manner, when T_{IN} at the input is too long, the OOT algorithm decreases t_{ON} from t_{ON4} to t'_{ON4} at an N_T between $N_{T\_\mathrm{MIN}}+1$ and $N_{T\_\mathrm{MAX}}-1$, thus reducing T_{IN} to T'_{IN}, as shown in Fig. 5(d), resulting in decreasing the input transient time. In this way, the OOT algorithm improves the regulation characteristics such as transient time and ripple voltage.

As described above, the OOT control method that adaptively adjusts t_{ON} required to energize the inductor in each *OP[3:0]* is proposed so as to secure the optimized t_{ON} according to harvesters and load conditions in all *OP[3:0]*. When more power is needed at the output load or when more power needs to be generated from the harvester, the same *OP[3:0]* is repeated. At this time, the proposed OOT algorithm increases t_{ON}, thus transferring more power to the output load or battery until the proposed SIMIMO converter operates in DCM, resulting in a high peak output and input power. When less power is needed at the output load or when less power needs to be generated from the harvester, *OP[3:0]* is no longer repeated. At this time, the proposed OOT algorithm decreases t_{ON}, thus transferring less power to the output load or battery, resulting in a high regulation characteristic. In this way, the OOT control method delivers more power to the output load, thus improving regulation characteristic. In addition, using the COT control method, the conduction loss or switching loss increases when t_{ON} is too long or too short, respectively [21]. In the proposed OOT control method, when t_{ON} is too long, t_{ON} is repeatedly adjusted by controlling N_T until t_{ON} is optimized, while preventing the occurrence of the undershoot and overshoot voltages at the output and input of the proposed converter, respectively, resulting in a less conduction loss. When t_{ON} is too short, t_{ON} is adjusted by controlling N_T as low as possible, thus not only improving the transient response and ripple voltage characteristics at the

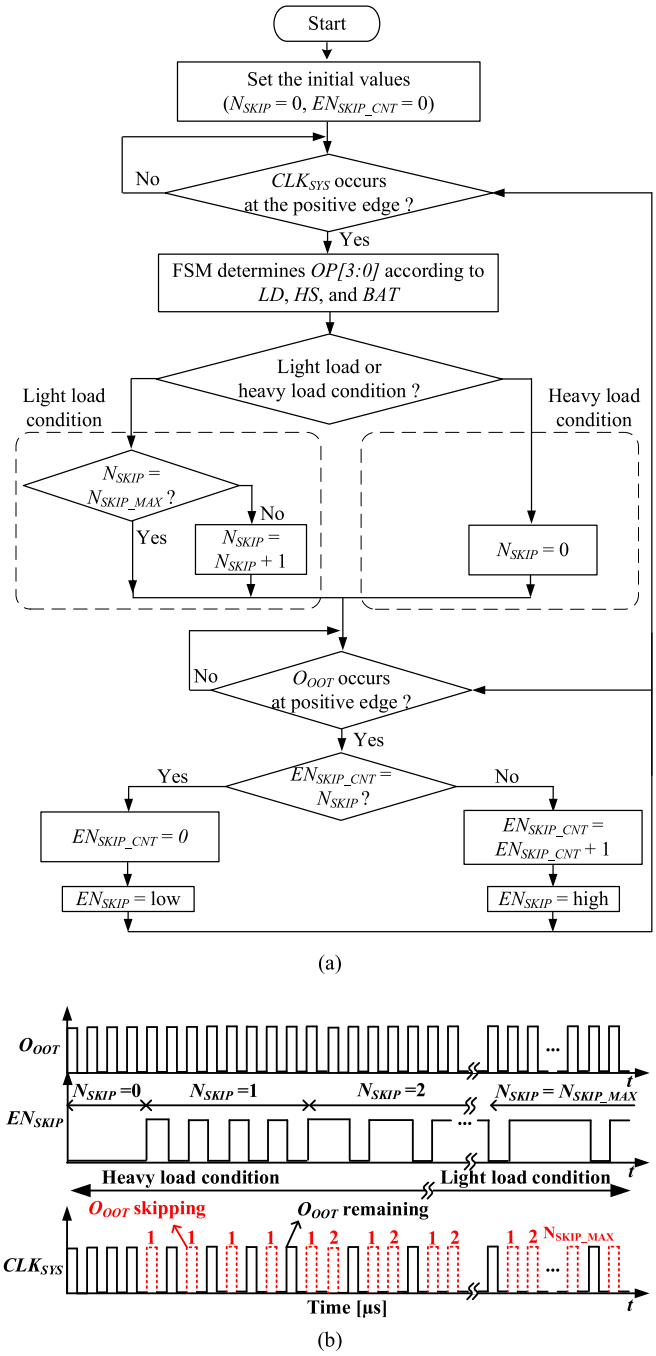

Fig. 6. (a) Flowchart and (b) timing diagram of the proposed skipping algorithm.

output, but also achieving less switching loss. In this way, the proposed OOT control method optimizes t_{ON}, while minimizing the conduction loss and switching loss as well as improving the power conversion efficiency.

C. Skipping Algorithm

Fig. 6(a) and (b), respectively, shows the flowchart and timing diagram of the proposed skipping algorithm, which optimally controls the number of O_{OOT} skippings according to the load condition in order to optimize the power consumption and regulation characteristics. The skipping algorithm starts with the initial values ($N_{\mathrm{SKIP}} = 0$, $EN_{\mathrm{SKIP\_CNT}} = 0$), where N_{SKIP} is the number of O_{OOT}s to be skipped, and $EN_{\mathrm{SKIP\_CNT}}$ is the number of the skipped O_{OOT}s. It is performed according to the load condition, which is determined by *OP[3:0]*.

Under the light-load condition, N_{SKIP} increases by 1 until it becomes equal to a maximum $N_{\mathrm{SKIP\_MAX}}$), which is determined according to CLK_{SYS} for preventing audible noise, thus decreasing the number of CLK_{SYS} occurrences, resulting in a reduction in the power consumption.

Under the heavy-load condition, N_{SKIP} becomes zero, thus increasing the number of CLK_{SYS} occurrences, resulting in a fast transient response for load regulation.

After increasing or decreasing N_{SKIP} under the light-load or heavy-load condition, respectively, $EN_{\mathrm{SKIP\_CNT}}$ is compared with N_{SKIP} at the positive edge of O_{OOT}. If $EN_{\mathrm{SKIP\_CNT}}$ is equal to N_{SKIP}, $EN_{\mathrm{SKIP\_CNT}}$ becomes 0 and the proposed skipping algorithm produces a low EN_{SKIP}, otherwise $EN_{\mathrm{SKIP\_CNT}}$ increases by 1 and the proposed skipping algorithm produces a high EN_{SKIP}. As shown in Fig. 6(b), depending on whether EN_{SKIP} is high or low, the O_{OOT} is skipped or not, respectively, and in addition, the O_{OOT} remaining after skipping is used as CLK_{SYS}. In this way, the proposed skipping algorithm minimizes the power consumption under the light-load condition and maximizes the regulation characteristics under the heavy-load condition by increasing (or decreasing) N_{SKIP} under the light- or heavy-load condition using the EN_{SKIP} signal, which controls the OOT generator.

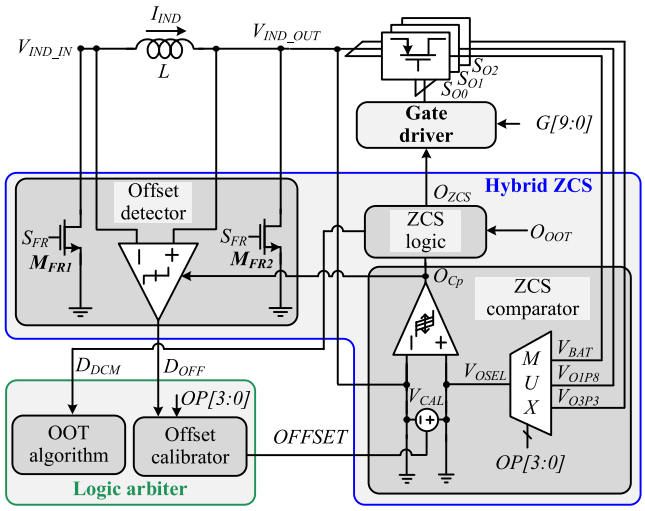

Fig. 7. Block diagram of the proposed hybrid ZCS.

IV. Hybrid ZCS With Offset Calibration

A. Operational Principle of Hybrid ZCS

Fig. 7 shows the block diagram of the hybrid ZCS in the PMC, which consists of a ZCS comparator, ZCS logic, and offset detector. The proposed hybrid ZCS turns ON one of S_{O0}–S_{O2} (S_{OSEL}), which is an output switch selected according

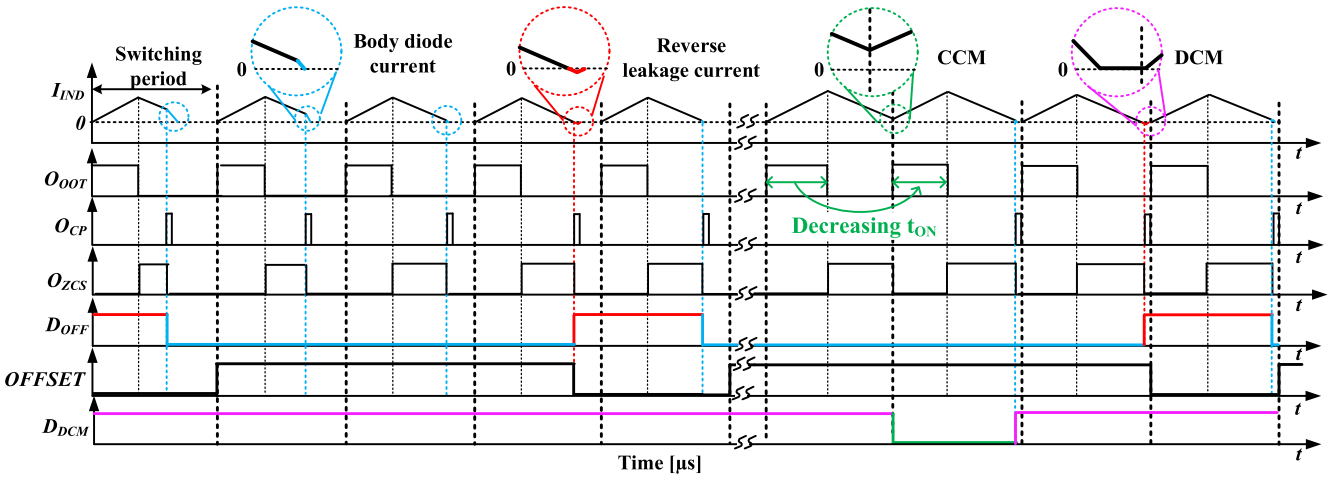

Fig. 8. Timing diagram of the proposed hybrid ZCS.

to *OP[3:0]*, when the I_{IND} starts to de-energize the inductor, and thus the energy can be transferred to the output load. Also, it turns OFF S_{OSEL} when the I_{IND} becomes zero, and thus the energy is no longer transferred to the output load.

The ZCS comparator compares the output voltage of the inductor $(V_{\mathrm{IND\_OUT}})$ with V_{OSEL} to detect the moment when the I_{IND} becomes zero, where V_{OSEL} is a voltage selected from among V_{O1P8}, V_{O3P3}, and V_{BAT} according to *OP[3:0]*. When the ZCS comparator detects the exact moment when the I_{IND} becomes zero, its output (O_{CP}) becomes high; otherwise, it becomes low. However, the ZCS comparator cannot detect such an exact moment due to its positive or negative offset voltage, which can be caused by the process variation or device mismatch. This offset voltage causes a body diode current or reverse leakage current, thus decreasing the power conversion efficiency. To solve the above problem, the offset detector and offset calibrator are implemented in the hybrid ZCS.

The offset detector detects the positive or negative offset voltage of the ZCS comparator, which occurs when the ZCS comparator operates before or after the I_{IND} becomes zero, respectively. When the positive offset voltage is detected, the I_{IND} flows through M_{FR1} and M_{FR2} in a clockwise direction, and the output of the offset detector (D_{OFF}) becomes low. In the same way, when the negative offset voltage is detected, the I_{IND} flows through M_{FR1} and M_{FR2} in a counterclockwise direction, and D_{OFF} becomes high. According to D_{OFF}, such an above positive or negative offset voltage can be calibrated by adjusting a calibration voltage (V_{CAL}) at the input of the ZCS comparator, which is controlled by *OFFSET* provided from the offset calibrator. If D_{OFF} is low, the positive offset voltage is negatively biased by enabling *OFFSET*, whereas if D_{OFF} is high, the negative offset voltage is positively biased by disabling *OFFSET*. In this way, the proposed hybrid ZCS can accurately detect the exact moment when the I_{IND} becomes zero by adaptively calibrating the positive or negative offset, resulting in improving the power conversion efficiency of the proposed SIMIMO converter.

The ZCS logic drives the gate driver to turn S_{OSEL} ON or OFF according to O_{OOT} and O_{CP}. When O_{OOT} is deactivated, the output of the ZCS logic (O_{ZCS}) becomes high, and then S_{OSEL} is turned ON. When O_{CP} is high or O_{OOT} is activated, O_{ZCS} becomes low, and then, S_{OSEL} is turned OFF. Here, since the I_{IND} becomes zero in DCM during the switching period, S_{OSEL} is turned OFF by a high O_{CP}, whereas since the I_{IND} does not become zero in CCM during the switching period, S_{OSEL} is turned OFF by an activated O_{OOT}. Thus, depending on whether S_{OSEL} is turned OFF by O_{CP} or O_{OOT}, the ZCS logic determines the proposed converter operation as in DCM or in CCM, and produces its output (D_{DCM}) high or low, respectively. When D_{DCM} is low in CCM, the proposed OOT algorithm in the logic arbiter limits the maximum register values of *OP[3:0]*, thus making the proposed converter always operate in DCM, resulting in high peak harvested input power and the peak output power in DCM. In this way, the proposed hybrid ZCS efficiently controls the energy transfer operation by turning on or off S_{OSEL} according to *OP[3:0]*.

Fig. 8 shows the timing diagram of the proposed hybrid ZCS. The I_{IND} increases when O_{OOT} is activated, whereas decreases when O_{ZCS} is high. When the positive offset voltage occurs at the input of the ZCS comparator, O_{CP} becomes high before the I_{IND} becomes 0, thus causing a body diode current. At this moment, the offset detector detects the positive offset voltage and makes D_{OFF} low by flowing the I_{IND} through M_{FR1} and M_{FR2} in a clockwise direction. Then, the offset calibrator enables *OFFSET* to calibrate the positive offset voltage by adjusting V_{CAL}. When the negative offset voltage occurs at the input of the ZCS comparator, O_{CP} becomes low after the I_{IND} becomes 0, thus causing a reverse leakage current. At this moment, the offset detector detects the negative offset voltage and makes D_{OFF} high by flowing the I_{IND} through M_{FR1} and M_{FR2} in a counterclockwise direction. Then, the offset calibrator disables *OFFSET* to calibrate the negative offset voltage by adjusting V_{CAL}. In this way, the offset calibration is performed by adaptively tracking whether the offset voltage is negative or positive, thus minimizing the offset voltage of the ZCS comparator.

In addition, when O_{OOT} is activated before the I_{IND} becomes zero, the ZCS logic considers the proposed converter as in CCM and makes both O_{ZCS} and D_{DCM} low. At this moment, the OOT algorithm decreases t_{ON} by adjusting the register value of *OP[3:0]*, as described in Section III.B, and thus O_{OOT} is activated after the I_{IND} becomes zero and D_{DCM} becomes high, representing that the proposed converter operates in DCM. In this way, D_{DCM} controls the OOT algorithm and makes the proposed converter always operate in DCM.

V. Circuit Implementation of the SIMIMO Converter

This section presents how the key circuit elements in the proposed SIMIMO converter are determined and implemented. The proposed SIMIMO converter, which employs a buck–boost converter structure to regulate V_{O3P3} and V_{O1P8}, is designed to operate at a default CLK_{SYS} frequency of 100 kHz. Here, CLK_{SYS} is determined to be greater than 25 kHz to prevent audible noise, and therefore $N_{\mathrm{SKIP\_MAX}}$ in the skipping algorithm is set to 4.

The minimum capacitance value of the output capacitor (C_{MIN}) is determined by the maximum load current at an N_{SKIP} of $N_{\mathrm{SKIP\_MAX}}$, while a target undershoot voltage is determined to be less than 10% of 1.8 V at V_{O3P3} or 3.3 V at V_{O1P8}. Thus, C_{MIN} can be obtained by

$$Q = C_{\mathrm{MIN}} V_{\mathrm{UNDERSHOOT}} = I_{\mathrm{MAX\_LOAD}} T_{\mathrm{CLK\_SKIP\_MAX}} \tag{1}$$

$$C_{\mathrm{MIN}} = \frac{I_{\mathrm{MAX\_LOAD}} T_{\mathrm{CLK\_SKIP\_MAX}}}{V_{\mathrm{UNDERSHOOT}}} \tag{2}$$

where $I_{\mathrm{MAX\_LOAD}}$, $T_{\mathrm{CLK\_SKIP\_MAX}}$, and $V_{\mathrm{UNDERSHOOT}}$ are the target maximum load current, period of the CLK_{SYS} when the number of skippings is in maximum, and target undershoot voltage of the proposed converter, respectively. Using (2), both C_{1P8} and C_{3P3} are determined to be 22 μF.

In addition, the inductance value of the inductor (L) is determined using $I_{\mathrm{IND\_PEAK}}$. When the inductor is energized during t_{ON}, the $I_{\mathrm{IND\_PEAK}}$ and peak output power for load ($P_{\mathrm{PEAK\_OUTPUT}}$) in DCM can be expressed as

$$I_{\mathrm{IND\_PEAK}} = \frac{V_{\mathrm{IN}}}{L} t_{\mathrm{ON}} \tag{3}$$

$$P_{\mathrm{PEAK\_OUTPUT}} \propto \frac{I_{\mathrm{IND\_PEAK}}}{2} V_{\mathrm{OUT}}. \tag{4}$$

Thus, as L decreases, both $I_{\mathrm{IND\_PEAK}}$ and $P_{\mathrm{PEAK\_OUTPUT}}$ increase. However, as $I_{\mathrm{IND\_PEAK}}$ increases in DCM, more conduction loss is induced. Therefore, $I_{\mathrm{IND\_PEAK}}$ should be optimally determined not only to minimize the conduction loss, but also to achieve the peak output power in DCM. Therefore, the minimum value of L that satisfies a target peak output power should be determined considering a margin in $P_{\mathrm{PEAK\_OUTPUT}}$. In this article, an L of 22 μH is selected considering a target $P_{\mathrm{PEAK\_OUTPUT}}$ of greater than 400 mW.

The capacitance value of the input capacitor (C_{IN}) is determined by the MPPT accuracy, which depends on the charging ability of the input capacitor during the sampling time of the open circuit voltage ($T_{\mathrm{OC\_SAMPLE}}$). Fig. 9(a) and (b) shows the timing diagram of V_{OC} according to C_{IN} and the equivalent circuit of the harvester, respectively. As shown in Fig. 9(a), the harvester charges the input capacitor up to V_{OC} during $T_{\mathrm{OC\_SAMPLE}}$. As C_{IN} increases, the ripple voltage at the input decreases, but the error in sampling V_{OC} increases, and thus the input harvester cannot fully charge the input capacitor up to V_{OC} during $T_{\mathrm{OC\_SAMPLE}}$, resulting in a decrease in the MPPT accuracy.

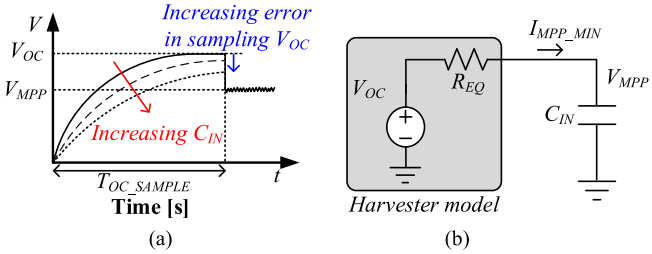

Fig. 9. (a) Timing diagram of open-circuit voltage sensing according to C_{IN} and (b) equivalent circuit of harvester.

Fig. 9(b) shows the equivalent resistance of the harvester (R_{EQ}), which can be expressed as

$$R_{EQ} = \frac{(V_{OC} - V_{\mathrm{MPP}})}{I_{\mathrm{MPP\_MIN}}} \tag{5}$$

where $I_{\mathrm{MPP\_MIN}}$ is the minimum input current when the input harvester has a minimum power. Thus, the allowable maximum C_{IN} ($C_{\mathrm{IN\_MAX}}$), which has a minimum error in sampling V_{OC}, can be derived as

$$C_{\mathrm{IN\_MAX}} = \frac{T_{OC\_\mathrm{SAMPLE}}}{R_{EQ}}. \tag{6}$$

In this article, the target $T_{\mathrm{OC\_SAMPLE}}$ and minimum harvested input power are set to 256 ms and 10 μW, respectively, and the capacitance value of all the input capacitors (C_{B1}–C_{B4}) is accordingly determined to be 4.7 μF using (5) and (6).

The input power switches for the harvesters (S_{I1}–S_{I4}) are implemented with transmission gates instead of using NMOS or PMOS, and thus the proposed SIMIMO converter can have a wide input range. The design parameters and specifications of the proposed SIMIMO converter are listed in Table I.

VI. Experimental Results

Fig. 10 shows a chip photomicrograph of the proposed SIMIMO converter with the PMC, which was fabricated using 0.18-μm standard bipolar-CMOS-DMOS process technology.

In the measurement, Keithely 2400 source meters and a model 2308 portable device battery charger simulator were used to measure the harvested input power and output power, and the battery charging and discharging power, respectively. The PRODIGIT 3332F electric load was used to control the load current. The harvester inputs were connected in series to the dc and rectified dc voltage sources through resistors. The high efficiently rectifier for piezoelectric and RF is shown in [31] and [32]. In [31], the high peak-to-peak ac voltage is rectified by

TABLE I
DESIGN PARAMETERS OF THE PROPOSED SIMIMO CONVERTER

Symbol	Description	VALUE
$f_{CLK\ SYS}$	System clock frequency	25-100 kHz
L	Inductor of the SIMIMO converter 7.2 mm x 7.2 mm x 4.8 mm (width x length x height)	22 μH (@ ESR : 61mΩ)
C_{B1}–C_{B4}	Input capacitors for harvesters	4.7 μF
C_{O1P8}	Output capacitor for V_{O1P8}	22 μF
C_{O3P3}	Output capacitor for V_{O3P3}	22 μF
V_{O3P3}	Output voltage of the SIMIMO converter	3.3V
V_{O1P8}	Output voltage of the SIMIMO converter	1.8V
V_{BAT}	Battery voltage	2.8-4.2 V

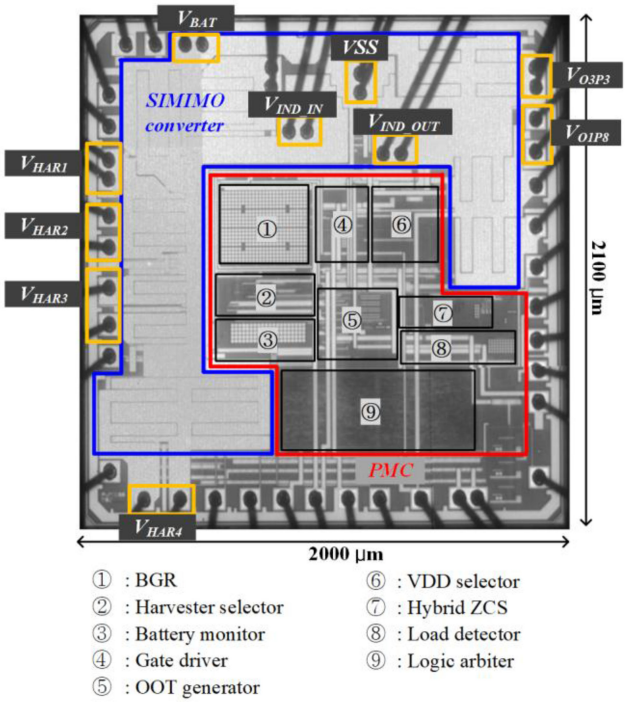

Fig. 10. Chip photomicrograph of the proposed SIMIMO converter with PMC.

changing the flow of inductor current using peak detector. In addition, the threshold-compensated method is used to rectify ac voltage with minimizing the turn-ON voltage of diode in [32]. Therefore, the dc or rectified dc voltage source is used to verify the performance of proposed SIMIMO converter since this work focuses on high peak and high efficiency power deliver from input to output. Here, the voltage values of the above dc voltage sources were determined according to the electric characteristics of harvesters specified in [24]–[27], and resistors were used to limit the harvester power.

Fig. 11(a) and (b), respectively, show the measured load transient waveforms at V_{O1P8} and V_{O3P3}, representing the regulation characteristics when the load currents at V_{O1P8} (I_{O1P8}) and V_{O3P3} (I_{O3P3}) vary from 100 μA to 130 mA and vice versa. The ripple voltages were measured to be 76 mV at V_{O1P8}, and

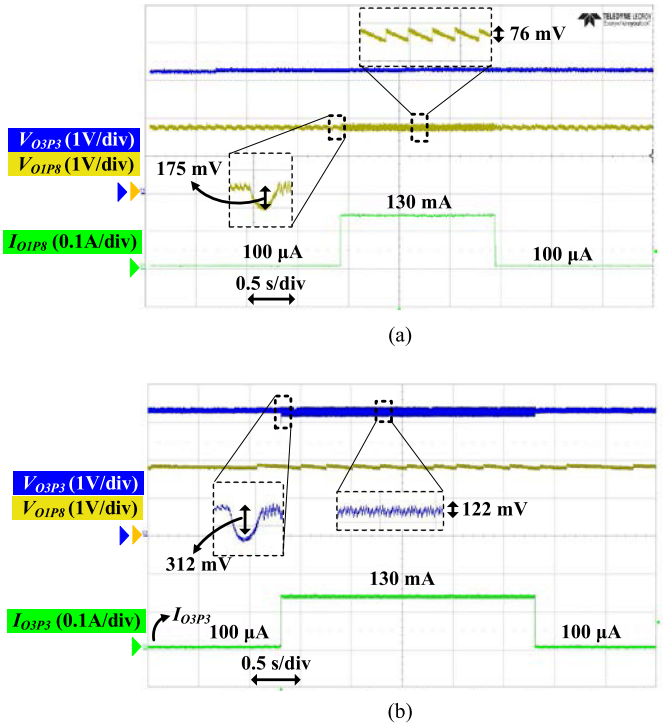

Fig. 11. Measured load transient waveforms at (a) V_{O1P8} and (b) V_{O3P3} when the load currents vary from 100 μA to 130 mA and vice versa.

122 mV at V_{O3P3}. The load regulation can be expressed as

$$Load\ regulation = \left(\frac{\Delta V_{OUT}}{\Delta V_{Load}}\right) \tag{7}$$

where ΔI_{OUT} is the change in the load current at V_{O1P8} (or V_{O3P3}), and ΔV_{OUT} is the change in V_{O1P8} (or V_{O3P3}). Using (7), the load regulations were calculated to be 1.5 mV/mA at V_{O1P8}, and 2.3 mV/mA at V_{O3P3}. In addition, the undershoot voltages were measured to be 175 mV at V_{O1P8} and 312 mV at V_{O3p3}, which were less than 10% of 1.8 and 3.3 V, respectively, in the worst case. These measurement results demonstrate that the proposed OOT and skipping algorithms properly reduced the undershoot voltages at the output load, and successfully achieved a target undershoot voltage, which is less than 10% of the supply voltage.

Fig. 12(a) shows the measured waveform when the harvester input current varies between 1 and 100 mA, and the photovoltaic open circuit voltage (V_{OC_HAR1}) varies between 3 and 4 V. The measurement results show that the MPPT accuracies are 97.1% and 97.6%, and V_{HAR1} are regulated at 2.162 and 2.867 V, at $V_{\mathrm{OC\_HAR1}}$ of 3 and 4 V, respectively. Here, the MPPT accuracy was calculated using

$$\mathrm{MPPT}\ accuracy = \left(1 - \frac{|V_{\mathrm{HAR\_MEASURED}} - V_{\mathrm{MPP\_IDEAL}}|}{V_{\mathrm{MPP\_IDEAL}}}\right) \times 100(\%) \tag{8}$$

where $V_{\mathrm{HAR\_MEASURED}}$ is the measured input voltage of the harvester, and $V_{\mathrm{MPP\_IDEAL}}$ is the ideal input voltage for

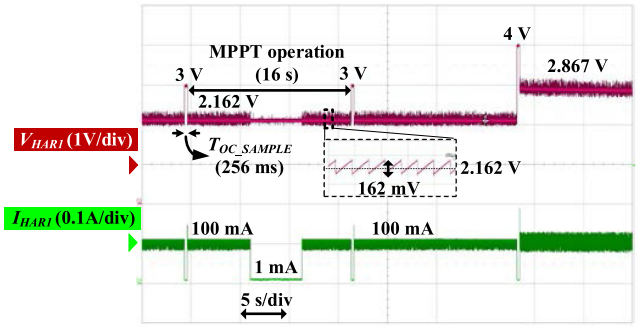

(a)

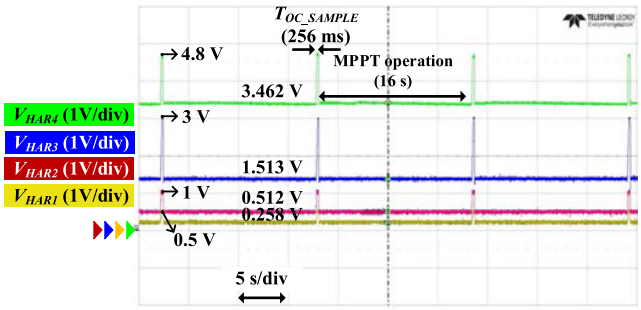

(b)

Fig. 12. Waveforms verifying MPPT operation (a) when the harvester input current and open-circuit voltage ($V_{\mathrm{OC\_}HAR1}$), respectively, vary between 1 and 100 mA and 3 and 4 V, and (b) when four harvesters are applied to the proposed converter.

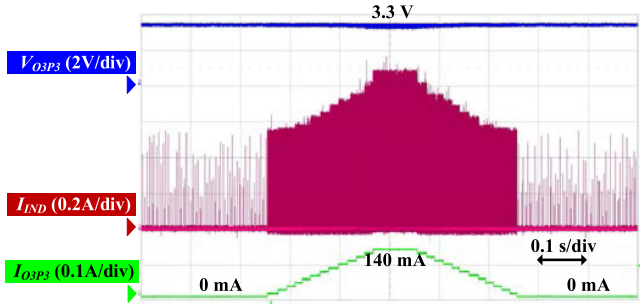

Fig. 13. Measured waveforms of the peak output power.

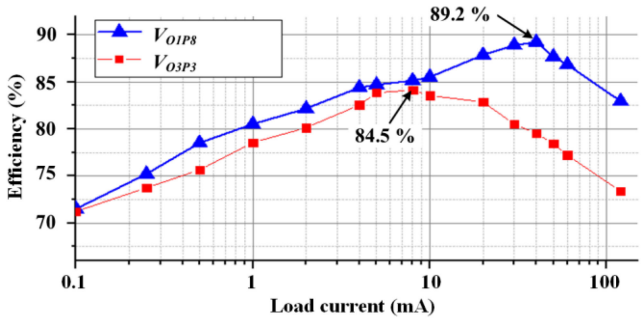

Fig. 14. Measured power conversion efficiency of V_{O3P3} and V_{O1P8} according to the load current when the harvested input power is zero and V_{BAT} is 4 V.

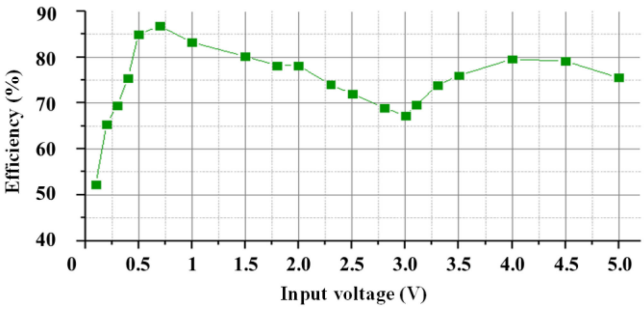

Fig. 15. Measured power conversion efficiency in charging the battery according to the harvester input voltage.

MPPT, which is obtained by sampling 70% or 50% of its V_{OC}, depending on the harvester type. These measurement results demonstrate that the proposed converter not only sensed V_{OC_HAR1} through proper MPPT operation, but also stably regulated V_{HAR1} even when the harvester input current and $V_{\mathrm{OC\_}HAR1}$ varied. Fig. 12(b) shows the measured waveform when four harvesters are applied to the proposed converter. When the dc input voltages of V_{HAR1}, V_{HAR2}, V_{HAR3}, and V_{HAR4}, which were 0.5, 1, 3, and 4.8 V, were applied to the proposed converter, the measured regulated V_{HAR1}, V_{HAR2}, V_{HAR3}, and V_{HAR4} were 0.258, 0.512, 1.513, and 3.462 V, as shown in Fig. 12(b), resulting in the MPPT accuracies of 96.8%, 97.6%, 99.1%, and 97.0%, respectively, which were calculated using (8). Here, V_{HAR1}, V_{HAR2}, V_{HAR3}, and V_{HAR4} are the modeled thermoelectric, RF, piezoelectric, and photovoltaic harvesters, respectively. These measurement results demonstrate that all the harvesters properly worked in MPPT, even when they operated simultaneously, representing that the proposed SIMIMO converter is suitable for multi-input energy harvesting systems.

Fig. 13 shows the measured peak output power when the load current at V_{O3P3} was increased up to 140 mA. This measurement result shows that the peak output power was achieved to be 462 mW, which was obtained by multiplying a V_{O3P3} of 3.3 V by an I_{O3P3} of 140 mA, demonstrating that the proposed OOT algorithm well achieved a target peak output power of greater than 400 mW.

Fig. 14 shows the measured power conversion efficiency of the proposed SIMIMO converter according to the load current when the harvester input voltage and V_{BAT} were zero and 4 V, respectively. The measurement results show that the peak power conversion efficiency of V_{O1P8} and V_{O3P3} was achieved to be 89.2% and 84.5%, respectively. In addition, Fig. 15 shows the measured power conversion efficiency in charging the battery according to the harvester input voltage when the load current at both V_{O1P8} and V_{O3P3}, the harvested input power, and V_{BAT} were 0 mA, 1 mW, and 4 V, respectively. The measured maximum and minimum power conversion efficiencies were achieved to be 86.4% at a V_{HAR1} of 0.7 V and 72.9% at a V_{HAR1} of 3 V, respectively. The above power conversion efficiencies differ due to the different ON-resistance values of the transmission gates at V_{HAR1} of 0.7 and 3 V, respectively. Therefore, Figs. 14 and 15

TABLE II
CONDUCTION LOSS AND SWITCHING LOSS IN POWER CONVERSION OF V_{O3P3}, V_{O1P8}, AND BATTERY CHARGING

Conversion efficiency	Type	Description
V_{O1P8}	Switching loss	$[(C_{G\_I0}V^2_{VDD} + C_{G\_DN}V^2_{VDD} + C_{G\_O1}V^2_{VDD})f_{SW}]$
	Conduction loss	$[t_{ON}(\frac{I_{IND\_PEAK}}{\sqrt{3}})^2(R_{ON\_I0}) + t_{OFF}(\frac{I_{IND\_PEAK}}{\sqrt{3}})^2(R_{ON\_DN}) + (t_{ON}+t_{OFF})(\frac{I_{IND\_PEAK}}{\sqrt{3}})^2(R_{ON\_O1}+R_{L\_ESR})]$
V_{O3P3}	Switching loss	$[(C_{G\_I0}V^2_{VDD} + C_{G\_EN}V^2_{VDD} + C_{G\_O2}V^2_{VDD} + C_{G\_DN}V^2_{VDD})f_{SW}]$
	Conduction loss	$[t_{ON}(\frac{I_{IND\_PEAK}}{\sqrt{3}})^2(R_{ON\_I0}+R_{ON\_EN}) + t_{OFF}(\frac{I_{IND\_PEAK}}{\sqrt{3}})^2(R_{ON\_DN}+R_{ON\_O2}) + (t_{ON}+t_{OFF})(\frac{I_{IND\_PEAK}}{\sqrt{3}})^2(R_{L\_ESR})]$
Charging battery	Switching loss	$[(C_{G\_I1-4}V^2_{VDD} + C_{G\_EN}V^2_{VDD} + C_{G\_O0}V^2_{VDD} + C_{G\_DN}V^2_{VDD})f_{SW}]$
	Conduction loss	$[t_{ON}(\frac{I_{IND\_PEAK}}{\sqrt{3}})^2(R_{ON\_I1-4}+R_{ON\_EN}) + t_{OFF}(\frac{I_{IND\_PEAK}}{\sqrt{3}})^2(R_{ON\_O0}+R_{ON\_DN}) + (t_{ON}+t_{OFF})(\frac{I_{IND\_PEAK}}{\sqrt{3}})^2(R_{L\_ESR})]$

C_{G_IO}–C_{G_IO4}, C_{G_O0}–C_{G_O2}, C_{G_EN}, and C_{G_DN}: the gate capacitance of power switches (S_{I0}–S_{I4}, S_{O0}–S_{O2}, S_{EN}, and S_{DN}).
R_{ON_IO}–R_{ON_IO4}, R_{ON_O0}–R_{ON_O2}, R_{ON_EN}, and R_{ON_DN}: the ON-resistance of power switches (S_{I0}–S_{I4}, S_{O0}–S_{O2}, S_{EN}, and S_{DN}).

TABLE III
PERFORMANCE COMPARISON

	This work	[14] TPE	[16] JSSC	[21] JSSC	[22] ISSCC	[28] TCAS I	[29] JSSC	[30] ISSCC
Process (μm)	0.18	0.35	0.35	0.18	0.028	0.18	0.18	0.13
Architecture	SIMIMO	SIMISO*	SIMIMO	SIMIMO	SIMIMO	SIMIMO	SIMIMO	SISISO
On-time control method	OOT	AOT	AOT	COT	AOT	AOT	AOT	COT
Number of harvester types***	4 (DC)	1 (AC) 3 (DC)	1 (AC) 2 (DC)	1 (DC)	3 (DC)	1 (DC)	2 (DC)	1 (DC)
Input voltage range	Harvester (0.1 V—5 V) Battery (2.8 V—4.2 V)	Harvester (0.1 V—5 V)	Harvester (0.03 V—5 V) Battery (3.3 V)	Harvester (2.5 V) Battery (3 V)	Harvester (0.1 V—1 V) Battery (1.8 V)	Harvester (0.5 V —1.2 V)	Harvester (0.05 V—0.8 V) Battery (1.2 V)	Harvester (3.6 V) Battery (3V)
Input capacitor	4.7 μF	22 μF	100 μF	n.a.	n.a.	-	10 μF	n.a
Inductor	22 μH	10 mH	22 μH	10 μH	10 μH	4.7 μH	4.7 μH	4.7 μH
Peak power conversion efficiency	89.2%	89.6%	83%	83%	89%	74.6%	84.4%	92.3%
Output voltage	1.8 V (regulated), 3.3 V (regulated)	5 V (not regulated)	1.8 V (regulated)	1 V (regulated) 1.8 V (regulated)	0.4—1.4 V (regulated)	1.2—1.4 V (regulated)	0.5 V (regulated) 1.2 V (regulated)	1.8 V (regulated)
Peak output power	462 mW	2.12 mW	2.5 mW	10 mW	60 mW	18 mW	4 mW	15 mW

*SIMISO: single inductor multi-input single output.
**SISISO: single inductor single-input single output.

demonstrate that the proposed SIMIMO converter with the hybrid ZCS method well achieved a high power conversion efficiency. Table II shows the description of how the switching loss and conduction loss are calculated [31]. These switching and conduction losses affect the power conversion efficiency of V_{O3P3} and V_{O1P8} shown in Fig. 14, and the power conversion efficiency in charging the battery shown in Fig. 15.

Fig. 16 shows the quiescent current consumption breakdown of the blocks in the PMC: 32% for the logic arbiter, 25% for the OOT generator, 15% for the load detector, 12% for BGR, 8% for the hybrid ZCS, 5% for the harvester selector, and 3% for the other blocks, respectively, resulting in a total quiescent current consumption of 1.6 μA.

Table III shows the performance comparison of the proposed SIMIMO converter with other works. Compared with other

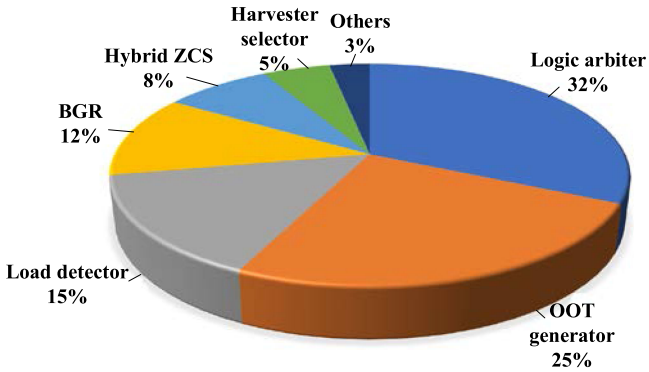

Fig. 16. Quiescent current consumption breakdown of the blocks in the PMC.

works, the proposed converter achieved the widest input and output voltage ranges, the largest peak output power, and high peak power efficiency, and thereby can be applied for a wide range of IoT applications. The work in [14] achieved a slightly higher power efficiency than the proposed converter. However, it requires an additional dc–dc converter or a low dropout regulator for regulation, thus occupying more area and decreasing the power conversion efficiency. In addition, the work in [30] achieved a slightly higher power efficiency of 93%, but had a very low peak output power of 15 mW and moreover could only be used for applications with the fixed input voltage and output voltage due to the use of the COT control method. Accordingly, the work achieved in [30] is not suitable for IoT applications such as LoRa and NB-IoT, which require high peak output power.

VII. Conclusion

This article proposes a high peak output power and high power conversion efficiency SIMIMO converter for energy harvesting systems. The proposed SIMIMO converter employs an OOT control method and a hybrid ZCS method. The proposed OOT control method optimally adjusts the on time required to energize the inductor, thus improving the input and output regulation characteristics, and increasing the peak output power for output loads, which is important for IoT applications requiring a wide distance range coverage. In addition, the proposed hybrid ZCS method adaptively calibrates the offset voltage of the ZCS comparator, thus achieving the high power conversion efficiency. The measurement result shows that the output power of the proposed converter was achieved to be 462 mW. The ripple voltages and load regulations at 1.8 V output and 3.3 V output were measured to be 76 mV and 1.5 mV/mA, and 122 mV and 2.3 mV/mA, respectively. The measured peak power conversion efficiency at 1.8 V output, 3.3 V output, and battery was 89.2%, 84.5%, and 86.4%, respectively. In addition, the measured quiescent current of the PMC was only 1.6 μA. Compared with previous works, the proposed converter achieved the widest input and output voltage ranges, and the highest peak output power. In addition, it achieved comparably high power conversion efficiency without requiring an additional dc–dc converter or a low dropout regulator for regulation. Therefore, the proposed SIMIMO converter with the PMC is suitable for energy harvesting systems in various IoT applications that require high peak output power, high power conversion efficiency, high regulation characteristics, and low power consumption.

References

[1] H. Erdem and V. Gungor, "On the lifetime analysis of energy harvesting sensor nodes in smart grid environments," *Ad Hoc Netw.*, vol. 75, pp. 98–105, 2018.

[2] W. Ejaz, M. Naeem, A. Shahid, A. Anpalagan, and M. Jo, "Efficient energy management for the Internet of Things in smart cities," *IEEE Commun. Mag.*, vol. 55, no. 1, pp. 84–91, Jan. 2017.

[3] Z. Sheng, C. Zhu, and V. C. M. Leung, "Surfing the Internet-of-Things: Lightweight access and control of wireless sensor networks using industrial low power protocols," *EAI Endorsed Trans. Ind. Netw. Intell. Syst.*, vol. 14, no. 1, 2014, Art. no. e2.

[4] T. Bouguera, J.-F. Diouris, J.-J. Chaillout, R. Jaouadi, and G. Andrieux, "Energy consumption model for sensor nodes based on LoRa and LoRaWAN," *Sensors*, vol. 18, no. 7, 2018, Art. no. 2104.

[5] J. de Carvalho Silva, J. J. P. C. Rodrigues, A. M. Alberti, P. Solic, and A. L. L. Aquino, "LoRaWAN—A low power WAN protocol for internet of things: A review and opportunities," in *Proc. Int. Multidisciplinary Conf. Comput. Energy Sci.*, 2017, pp. 1–6.

[6] M. Lauridsen, R. Krigslund, M. Rohr, and G. Madueno, "An empirical NB-IoT power consumption model for battery lifetime estimation," in *Proc. IEEE 87th Veh. Tech. Conf.*, Porto, Portugal, Jun. 2018, pp. 1–5.

[7] S. Höfle, A. Schienle, C. Bernhard, M. Bruns, U. Lemmer, and A. Colsmann, "Solution processed, white emitting tandem organic light-emitting diodes with inverted device architecture," *Adv. Mater.*, vol. 26, no. 30, pp. 5155–5159, Aug. 2014.

[8] Y. K. Ramadass and A. P. Chandrakasan, "A batteryless thermoelectric energy-harvesting interface circuit with 35 mV startup voltage," *IEEE J. Solid -State Circuits*, vol. 46, no. 1, pp. 333–341, Jan. 2011.

[9] D. Kwon and G. A. Rincon-Mora, "A single-inductor 0.35 μm CMOS energy-investing piezoelectric harvester," in *Proc. IEEE Int. Solid-State Circuits Conf. Dig. Tech.*, 2013, pp. 78–80.

[10] H. Jabbar, Y. S. Song, and T. T. Jeong, "RF energy harvesting system and circuits for charging of mobile devices," *IEEE Trans. Consum. Electron.*, vol. 56, no. 1, pp. 247–253, Feb. 2010.

[11] Y. K. Tan and S. K. Panda, "Energy harvesting from hybrid indoor ambient light and thermal energy sources for enhanced performance of wireless sensor nodes," *IEEE Trans. Ind. Electron.*, vol. 58, no. 9, pp. 4424–4435, Sep. 2011.

[12] Y.-K. Teh and P. K. T. Mok, "A stacked capacitor multi-microwatts source energy harvesting scheme with 86 mV minimum input voltage and $\pm$3 V bipolar output voltage," *IEEE J. Emerg. Sel. Topics Circuits Syst.*, vol. 4, no. 3, pp. 313–323, Sep. 2014.

[13] Y. Qiu, C. V. Liempd, B. O. Veld, P. G. Blanken, and C. V. Hoof, "5 μW-to-10 mW input power range inductive boost converter for indoor photovoltaic energy harvesting with integrated maximum power point tracking algorithm," in *Proc. IEEE Int. Solid-State Circuits Conf. Dig. Tech.*, Feb. 2011, pp. 118–120.

[14] M. Dini, A. Romani, M. Filippi, V. Bottarel, G. Ricotti, and M. Tartagni, "A nanocurrent power management IC for multiple heterogeneous energy harvesting sources," *IEEE Trans. Power Electron.*, vol. 30, no. 10, pp. 5665–5680, Oct. 2015.

[15] D. Ma, W. H. Ki, C. Y. Tsui, and P. K. T. Mok, "Single-inductor multiple output switching converters with time-multiplexing control in discontinuous conduction mode," *IEEE J. Solid-State Circuits*, vol. 38, no. 1, pp. 89–99, Jan. 2003.

[16] S. Bandyopadhyay and A. P. Chandrakasan, "Platform architecture for solar, thermal, and vibration energy combining with MPPT and single inductor," *IEEE J. Solid-State Circuits*, vol. 47, no. 9, pp. 2199–2215, Sep. 2012.

[17] N.-M. Sze, F. Su, Y.-H. Lam, W.-H. Ki, and C.-Y. Tsui, "Integrated single-inductor dual-input dual-output boost converter for energy harvesting applications," in *Proc. IEEE Int. Symp. Circuits*, 2008, pp. 2218–2221.

[18] P. H. Chen, C. Shiang, and K. C. Lin, "A 50 nW-to10 mW output power tri-mode digital buck converter with self-tracking zero current detection for photovoltaic energy harvesting," *IEEE J. Solid-State Circuits*, vol. 51, no. 2, pp. 523–532, Feb. 2016.

[19] R. D. Prabha and G. A. Rincón-Mora, "0.18-μm light-harvesting battery assisted charger-supply CMOS system," *IEEE Trans. Power Electron.*, vol. 31, no. 4, pp. 2950–2958, Apr. 2016.

[20] M. Chen and G. A. Rincón-Mora, "Single inductor, multiple input, multiple output power mixer–charger–supply system," in *Proc. Int. Symp. Low Power Electron. Des.*, Aug. 2007, pp. 301–315.

[21] G. Yu, K. W. R. Chew, Z. C. Sun, H. Tang, and L. Siek, "A 400 nW single-inductor dual-input–tri-output DC–DC buck–boost converter with maximum power point tracking for indoor photovoltaic energy harvesting," *IEEE J. Solid-State Circuits*, vol. 50, no. 11, pp. 2758–2772, Nov. 2015.

[22] S. S. Amin and P. P. Mercier, "MISIMO: A multi-input single-inductor multi-output energy harvester employing event-driven MPPT control to achieve 89% peak efficiency and a 60,000x dynamic range in 28 nm FDSOI," in *Proc. IEEE Int. Solid-State Circuits Conf. Dig. Tech.*, Feb. 2018, pp. 144–146.

[23] Y. Lu, S. Yao, S. Bin, and P. Brokaw, "A 200 nA single-inductor dual-input-triple-output (DITO) converter with two-stage charging and process-limit cold-start voltage for photovoltaic and thermoelectric energy harvesting," in *Proc. IEEE Int. Solid-State Circuits Conf. Dig. Tech.*, Feb. 2016, pp. 368–369.

[24] *Thin Film Thermogenerator*, Micropelt, MPG-D655 datasheet, Jun. 2014.

[25] *Power and Data Transmitter*, Powercast, TX91501-3W-ID datasheet, Jan. 2014.

[26] *Piezoelectric Energy Harvesters*, Mide Technol. Corporation, PPA-4011 datasheet, Jan. 2017.
[27] *Photovoltaic Cell*, IXYS, 2013. [Online]. Available: http://ixapps.ixys.com/DataSheet/KXOB22-01X8-DATA-SHEET-20110818-.pdf.
[28] H.-H. Wu, C.-H. Huang, C.-L. Wei, and J.-S. Lai, "Bidirectional single-inductor dual-supply converter with automatic state-transition for IoT applications," *IEEE Trans. Circuits Syst. I, Reg. Papers*, vol. 66, no. 10, pp. 4068–4078, Feb. 2019.
[29] C.-W. Liu, H.-H. Lee, P.-C. Liao, Y.-L. Chen, M.-J. Chung, and P.-H. Chen, "Dual-source energy-harvesting interface with cycle-by-cycle source tracking and adaptive peak-inductor-current control," *IEEE J. Solid-State Circuits*, vol. 53, no. 10, pp. 2741–2750, Oct. 2018.
[30] H.-J. Chen, Y.-H. Wang, P.-C. Huang, and T.-H. Kuo, "An energy recycling three-switch single-inductor dual-input buck/boost DC-DC converter with 93% peak conversion efficiency and 0.5 mm^2 active area for light energy harvesting," in *Proc. IEEE Int. Solid-State Circuits Conf. Dig. Tech. Papers*, Feb. 2015, pp. 1–3.
[31] R. W. Erickson and D. Maksimovic, *Fundamentals of Power Electronics*. New York, NY, USA: Springer, 2012.
[32] M. T. Penella and M. Gasulla, "A simple and efficient MPPT method for low-power PV cells," *Int. J. Photoenergy*, vol. 2014, Feb. 2014, Art. no. 153428.
[33] C. Ni and T. Tetsuo, "Adaptive constant ON-time (D-CAP) control study in notebook applications (application report no. SLVA281B)," Retrieved from Texas Instruments, 2007. [Online]. Available: http://www.ti.com/lit/an/slva281b/slva281b.pdf

Jae-Hyung Jung (Student Member, IEEE) received the B.S. degree in electronics and computer engineering in 2012 from Hanyang University, Seoul, South Korea, where he is currently working toward the Ph.D. degree in electronics and computer engineering.

His research interests include power management IC design for energy harvesting, battery chargers, and low dropout regulators.

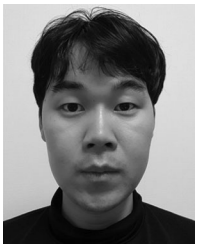

Young-Ho Jung (Member, IEEE) received the B.S. degree in electrical and computer engineering in 2009 and the combined M.S. and Ph.D. degrees in electronic engineering from Hanyang University, Seoul, Korea, in 2018.

Since 2018, he has been with Samsung Electronics, Hwaseong, South Korea, where he leads the development of supply modulator for an envelope tracking (ET) power management IC. His research interests include the design and analysis of a variety of switching-mode power converters for smart mobile device and home electronic appliances, single-inductor multioutput converters, battery chargers, energy-harvesting circuits, driving of LED backlights, and LED lightings.

Seong-Kwan Hong (Member, IEEE) received the B.S. degree in electronic engineering from Hanyang University, Seoul, South Korea, in 1980, and the M.S. and Ph.D. degrees in electrical engineering from the Georgia Institute of Technology, Atlanta, GA, USA, in 1985 and 1994, respectively.

From 1990 to 1995, he was with Cadence Design Systems, Inc., San Jose, USA, where he developed several ECAD products. In 1995, he joined R&D Lab of LG semicon, Seoul, where he was in charge of Design Technology Center as a Research Fellow. In 1999, he became the Vice President and Chief Information Officer with Hynix Semiconductor, Inc., where he was responsible for the information technology and R&D engineering support. From 2009 to 2013, he was with Yonsei University, Seoul, as a Hynix Chair & Research Professor. In 2013, he joined Hanyang University as a Research Professor. His research interests include EDA design methodology, mixed IC design, and automotive IC design.

Oh-Kyong Kwon (Member, IEEE) received the B.S. degree in electronic engineering from Hanyang University, Seoul, South Korea, in 1978, and the M.S. and Ph.D. degrees in electrical engineering from Stanford University, Stanford, CA, USA, in 1986 and 1988, respectively.

From 1987 to 1992, he was with the Semiconductor Process and Design Center, Texas Instruments, Inc., Dallas, TX, USA, where he was involved in the development of multichip module technologies and smart power integrated circuit technologies for automotive and flat panel display applications. In 1992, he joined Hanyang University as an Assistant Professor with the Department of Electronic Engineering, where he is currently a Professor. He has authored and coauthored more than 313 international journal and conference papers and 224 US patents. His research interests include interconnect and electrical noise modeling for high-speed system-level integration, wafer-scale chip-size packages, smart power integrated circuit technologies, mixed-mode signal circuit design, imagers, analog front-end circuit design for biomedical instruments, and the driving methods and circuits for flat panel displays.